Chemical Engineering Journal 375 (2019) 122055

Contents lists available at ScienceDirect

Chemical Engineering Journal

journal homepage: www.elsevier.com/locate/cej

Ultra-fine zinc oxide nanocrystals decorated three-dimensional macroporous polypyrrole inverse opal as efficient sulfur hosts for lithium/sulfur batteries

Yongguang Zhang[a], Weilong Qiu[a], Yan Zhao[a,*], Yong Wang[b], Zhumabay Bakenov[c], Xin Wang[d,*]

[a] School of Materials Science and Engineering, Hebei University of Technology, Tianjin 300130, China
[b] Dongguan South China Design Innovation Institute, Guangdong, China
[c] School of Engineering, Nazarbayev University, Institute of Batteries LLC, National Laboratory Astana, 53 Kabanbay Batyr Avenue, Astana 010000, Kazakhstan
[d] International Academy of Optoelectronics at Zhaoqing, South China Normal University, Guangdong, China

HIGHLIGHTS

- 3DOMPPy supported ultra-fine ZnO nanocrystals was prepared by hard-template method.
- The porous 3DOMPPy ensures high sulfur utilization and fast sulfur kinetics.
- The ZnO particles offer a strong chemical bonding with lithium polysulfides.
- The cell with S-3DOMPPy@ZnO composite exhibit enhanced cycling performance.

GRAPHICAL ABSTRACT

Schematic of preparation procedure of 3DOMPPy@ZnO and S-3DOMPPy@ZnO.

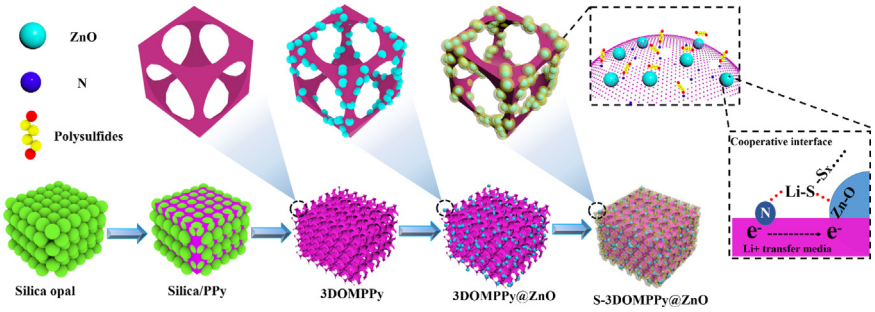

ARTICLE INFO

Keywords:
Lithium/sulfur battery
S-3DOMPPy@ZnO composite cathode
Three-dimensional porous polypyrrole
Ultrafine ZnO nanocrystals

ABSTRACT

Despite high theoretical capacity (1675 mAh g^{-1}) and low cost of the lithium/sulfur (Li/S) batteries, their industrial road is impeded by rapid capacity loss and poor rate performances caused by the dissolution of lithium intermediate in the electrolyte. In this work, a composite is reported, which consists of highly dispersed ultrafine (~5 nm) zinc oxide (ZnO) nanocrystals decorated on conductive three-dimensionally macroporous polypyrrole (3DOMPPy) inverse opal, for polysulfides immobilization in Li/S batteries. Compared with carbon matrixes, 3DOMPPy provides a stronger lithium polysulfides binding site, due to its unique macroporous structure. Through constructing 3D ordered macroporous structure of PPy, a fast electron transfer pathway and an efficient buffer space for sulfur are provided. Furthermore, polar ZnO can confine polysulfides greatly by chemical adsorption, which is verified by density functional theory calculations. Consequently, S-3DOMPPy@ZnO demonstrates durable long-term cyclability (794.5 mAh g^{-1} after 300 cycles at 0.1 C) as well as a remarkable rate capability (515.6 mAh g^{-1} at 2 C).

1. Introduction

With the ever-growing demands for rechargeable batteries, an explosive growth of next-generation energy storage technologies is strongly expected [1–3]. Recently, Li/S batteries has attracted a lot of attention because of high theoretical capacity (1675 mAh g^{-1}), low cost, and environmental benignity [4–6]. Nevertheless, several challenges still need to be solved before the large-scale practical

* Corresponding authors.
E-mail addresses: yanzhao1984@hebut.edu.cn (Y. Zhao), wangxin@scnu.edu.cn (X. Wang).

https://doi.org/10.1016/j.cej.2019.122055
Received 16 May 2019; Received in revised form 10 June 2019; Accepted 22 June 2019
Available online 24 June 2019
1385-8947/

applications of Li/S batteries systems [7–9]. First, sulfur and its insoluble discharge products are both electrically insulating, which limit the utilization of sulfur and lower the rate capability of Li/S batteries. Second, large volume variation of sulfur (~80%) causes hidden dangers for electrode structure stability. Thirdly, the "shuttle effect" caused by soluble lithium polysulfides (Li_2S_x, $4 \le x \le 8$) usually brings about poor cycling life, unsatisfactory rate performance.

Therefore, to address the mentioned problems, much effort has been expended over recent decades to explore the appropriate sulfur host materials. The introduction of carbon materials, including graphene [10], carbon nanotube [11], and micro/mesoporous carbon [12], regulated polysulfides dissolution/shuttling by physical confinement. Compared with carbon matrixes, polypyrrole (PPy) provides a stronger lithium polysulfides binding, due to its unique long chain conjugate structure and porous morphology [13]. Thus, a large number of PPy with diverse structure, such as nanotube [14], hollow nanosphere [15] and nanofiber [16], were recently reported to composite with sulfur, exhibiting an enhanced electrochemical performance.

Recent studies have revealed that the porous PPy matrix can not only provide obvious immobilization towards polysulfides, but also alleviate the volume change of sulfur during discharge/charge process [17]. However, a challenge for the application of porous PPy as a sulfur host is their high interfacial impedance due to the poor wettability of the porous PPy against lithium polysulfides, which causes a poor contact and leads to an inefficient interaction between porous PPy and lithium polysulfides.

To cope with these notorious posers, a composite, that consist of highly dispersed ultrafine (~5 nm) zinc oxide (ZnO) nanocrystals decorated on conductive three-dimensionally macroporous polypyrrole (3DOMPPy) inverse opal, is designed and synthesized in this work. Such elaborately designed 3DOMPPy@ZnO can synergistically combine the merits of three-dimensionally ordered macroporous polypyrrole and ZnO nanocrystals when used as for polysulfides immobilization of Li/S batteries. Specifically, ultrafine ZnO nanocrystals was high-dispersedly grown on the surface of 3DOMPPy, which could significantly improve the wettability between porous PPy and lithium polysulfides, and decrease the interface resistance. In addition, the large mesopores constructed from conductive PPy favors the rapid transport of Li ions as well as ensures a high and homogeneous loading of sulfur. What's more, polar ZnO suppresses the dissolution of polysulfides effectively by chemical adsorption, which is verified by density functional theory calculations.

2. Experimental methods

2.1. Preparation of SiO_2 sphere arrays

The SiO_2 sphere arrays were prepared by evaporating silica colloids solvent. Details on the preparation methods can be found in published literature [18]. Briefly, the silica colloids were obtained by stirring the mixture of 20 mL of tetraethyl orthosilicate (TEOS), 200 mL ethanol, and 20 mL of aqueous ammonia ($NH_3{\cdot}H_2O$) with 40 mL of deionized water for 12 h at 40 °C. Followed by evaporating the solvent at 70 °C for 24 h, the ordered silica sphere nano-arrays were collected. The diameters of the SiO_2 nanospheres was around 300 nm.

2.2. Synthesis of 3DOMPPy

The 3DOMPPy was achieved by using silica sphere nano-arrays as templates. The silica sphere nano-arrays were mixed with 200 mL of distilled water containing 2 g of hexadecyl trimethyl ammonium bromide (CTAB). Then, 0.5 g pyrrole monomer was slowly added into above solution followed by vigorously stirring for 2 h in an ice bath (0–5 °C). Subsequently, 60 mL of 0.15 mol/L $FeCl_3$ mixture was added dropwisely to the mentioned solution and maintained for 12 h. The product was centrifuged and washed repeatedly by distilled water. Finally, 5 wt% HF solution was employed to remove the SiO_2 sphere arrays. The resulting 3DOMPPy product was centrifuged, cleaned and dried at room temperature.

2.3. Synthesis of 3DOMPPy@ZnO and S-3DOMPPy@ZnO composite

The 3DOMPPy@ZnO composite was fabricated by an in situ solution method. Firstly, 3.0 g of $Zn(COOH)_2$ and 1.0 g of KOH were predissolved in 60 and 40 mL methyl alcohol, respectively. Then, well dispersed of 30 mL methyl alcohol containing 0.5 g 3DOMPPy mixed with as-prepared $Zn(COOH)_2$ solution kept stirring at 60 °C. Then, the as-prepared KOH solution was mixed with above solution and reacted for 2 h. The resulting powder was collected by centrifugation. Finally, the 3DOMPPy@ZnO was obtained by vacuum dry under 80 °C.

The S-3DOMPPy@ZnO was synthesized by a simple hydrothermal. Typically, 3DOMPPy@ZnO was mixed with commercial sulfur at mass ratio of 1:3 and poured into a Teflon-lined autoclave at 155 °C for 6 h.

2.4. Electrochemical measurements

The cathode was made by blending 80% S-3DOMPPy@ZnO, 10% acetylene black, and 10% polyvinylidene fluoride (PVDF), and dispersed in 1-methyl-2-pyrrolidinone (NMP) to form a homogeneous slurry. The resultant slurry was coated on carbon coating aluminum foil substrates with doctor blade, followed by drying in a vacuum oven at 60 °C for 12 h. Subsequently, the prepared electrode was cut into a circular disk and pressed at 8 MPa. Coin cells 2025 were assembled in a highly pure argon glove box (MBraun). Lithium metal and microporous polypropylene (Celgard 2400) served as anode and separator, respectively. The electrolyte is consisted of 1 M lithium bis(trifluoromethanesulfonyl)imide (LiTFSI) in dimethoxy ethane (DME) and 1,3-dioxolane (DOL) (1:1 v/v) with 0.1 M $LiNO_3$ as additive. The assembled cells were galvanostatically charged and discharged between 1.5 and 3.0 V versus vs. Li^+/Li at different current densities on a multichannel battery cycler (Neware CT-4008) testing system.

2.5. Material characterization

The crystalline structures of 3DOMPPy, 3DOMPPy@ZnO and S-3DOMPPy@ZnO were studied using an X-ray diffractometer (XRD, Smart Lab, Rigaku Corporation) with a Cu-Kα radiation. The architectures of the compound were observed by field emission scanning electron microscopy (SEM, S4800, Hitachi Limited). Transmission electron microscopy (TEM, JEM-2100F, JEOL) with energy dispersive spectroscopy (EDS) was employed to observe interior structure. The thermogravimetric analysis (TGA, SDT Q-600. TA Instruments-Waters LLC) was operated under air or N_2 flow with heating from 50 °C to 800 °C at 10 °C min^{-1}. Thermo Scientific K-Alpha XPS spectrometer was employed for X-ray photoelectron spectroscopy (XPS) with Al Kα X-ray source. Fourier transformation infrared spectra (FTIR, V80, Bruker Corporation) were analyzed the surface composition of the composites.

2.6. Theoretical calculations

The atomic configurations and binding energies were simulated using the VASP program according to the Density Theory Functional (DFT) calculations within the Perdew-Burke-Ernzerhof (PBE) exchange–correlation functional for Generalized Gradient Approximation (GGA). A planewave cutoff energy of 400 eV was used to describe the interactions. A 3×3 unit cell was employed to model the ZnO (1 0 1) surface with Li_2S_6. The structures were granted to relax until the forces acting on the atoms were less than 0.03 eV $Å^{-1}$ and the vacuum height was set to 15 Å.

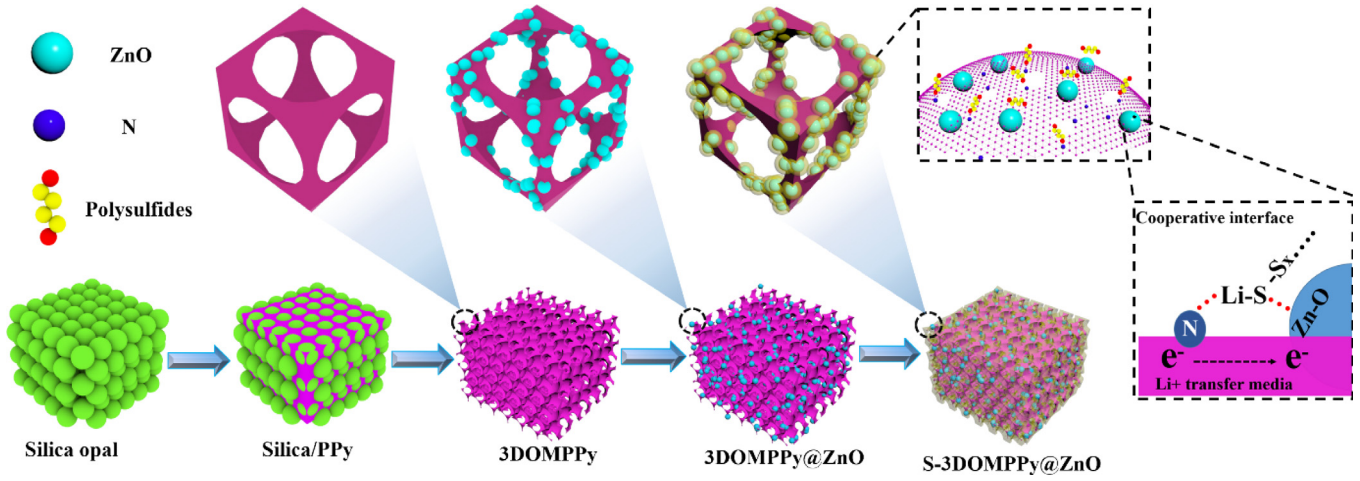

Fig. 1. Schematic of preparation procedure of 3DOMPPy@ZnO and S-3DOMPPy@ZnO.

3. Results and discussion

The overall synthetic procedure for S-3DOMPPy@ZnO was presented in Fig. 1. SiO_2 was used as sacrificial template to prepare 3DOMPPy, and ZnO was compounded to synthesize 3DOMPPy@ZnO by in-situ solution growth. Finally, the complexation of sulfur was achieved by simple hydrothermal reaction.

Fig. 2a showed the typical SEM image of 3DOMPPy, and an ordered macroporous structure over tens of microns can be observed. The higher magnification as shown in Fig. 2b revealed the size of the macropores is ca. 250 nm, which was smaller than the diameter of the original silica spheres, indicating the 3DOMPPy contract after the removal of the silica opal. The shrinkage of the 3DOMPPy was due to densitify by dehydration and solvent removal [18]. Fig. 2c revealed the SEM image of 3DOMPPy@ZnO composite, and from the image, the ordered macroporous structure was still well maintained after loading ZnO nanocrystals, which would facilitate the higher sulfur loading and charge transfer during the electrode reactions. To verify ZnO nanocrystals was uniformly deposited on the 3DOMPPy, EDS mapping was performed in the 3DOMPPy@ZnO composite (Fig. 2d). The bright spots

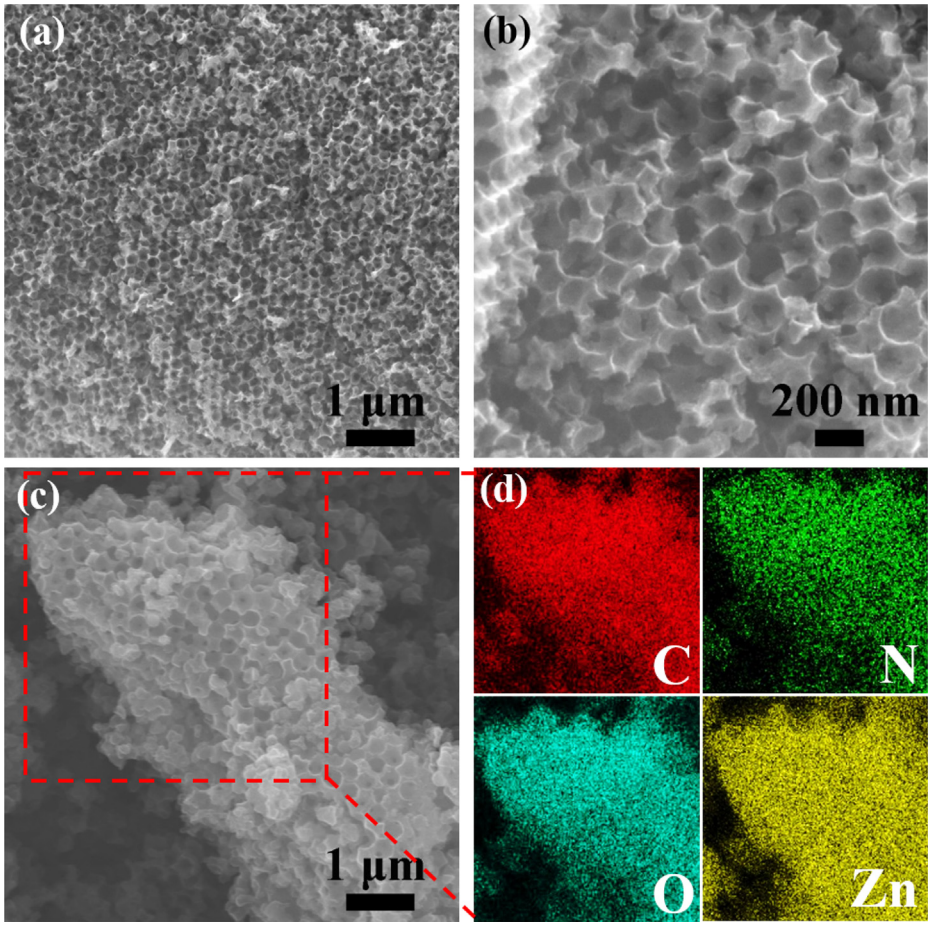

Fig. 2. SEM images of (a, b) 3DOMPPy with different magnifications; (c) 3DOMPPy@ZnO; (d) The corresponding element mapping of 3DOMPPy@ZnO.

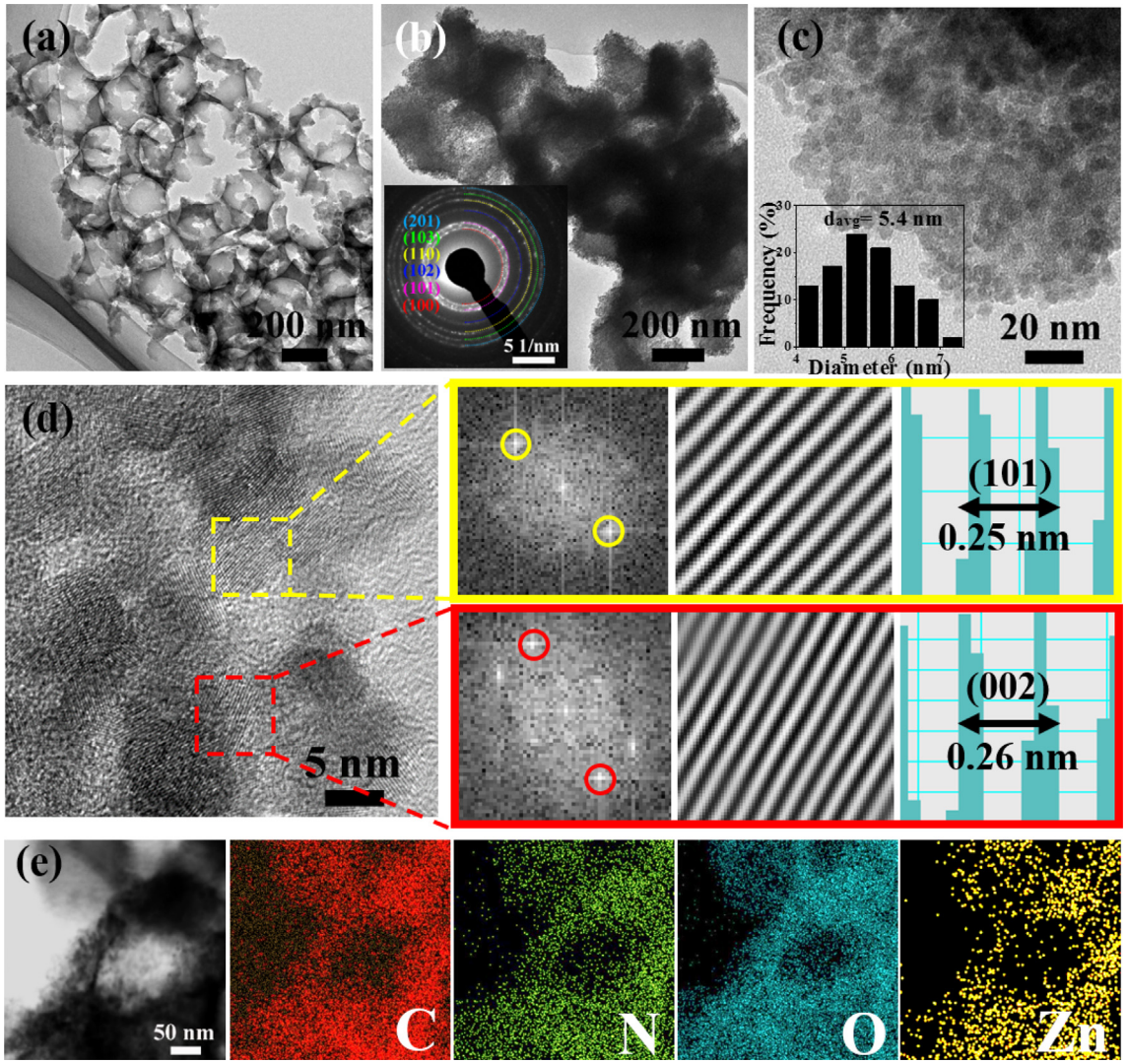

Fig. 3. TEM image of (a) 3DOMPPy; (b-c) 3DOMPPy@ZnO with different magnifications; (d) HRTEM and the corresponding FFT, inverse FFT, lattice spacing image of 3DOMPPy@ZnO; (e) 3DOMPPy@ZnO and corresponding element mapping.

corresponded to the presence of the elements of C, N, O and Zn, indicating ZnO nanocrystals were distributed uniformly throughout the whole area.

Fig. 3a displayed the TEM result of the as-prepared porous 3DOMPPy sample with macroporous pores of ~250 nm in diameter, where interconnected channels were evident. The arranged macropores and the associated channels benefited the loading of sulfur and shorten the transport length of ions. The successful growth of uniformly distributed ZnO crystals on 3DOMPPy were demonstrated in Fig. 3(b-c). Fig. 3b showed ZnO nanocrystals were successfully loading on 3DOMPPy without aggregation, and corresponding selected area electron diffraction (SAED) pattern (inset of Fig. 3b) revealed polycrystalline characteristics feature with homogenous diffraction rings, exhibiting a high crystallinity of ZnO nanocrystals. From Fig. 3c, the ZnO nanocrystals were uniformly dispersed on the macropore walls of the 3DOMPPy and the average size of the ZnO nanocrystals was about 5 nm based on nanocrystals randomly selected. The 3D porous structure of the 3DOMPPy@ZnO composite effectively confined the aggregation of ZnO nanocrystals [19]. The HRTEM of 3DOMPPy@ZnO composite was shown in Fig. 3d, the lattice fringes could be clearly calculated to be 0.25 nm of (1 0 1) plane and 0.26 nm of (0 0 2) plane for ZnO respectively. Fig. 3e showed TEM images of 3DOMPPy@ZnO composite and corresponding element mapping, which further confirmed ZnO was uniformly distributed throughout the 3DOMPPy.

Fig. 4a showed the XRD patterns of 3DOMPPy, 3DOMPPy@ZnO and S-3DOMPPy@ZnO composites. The 3DOMPPy exhibited a broad peak around 24.8°, which was a characteristic peak of amorphous polypyrrole [20]. Furthermore, the crystalline patterns of 3DOMPPy@ZnO exhibited diffraction peaks at 31.6°, 34.4°, 36.1°,47.6°, 56.6°, 62.9° and 67.8°, which can be assigned to ZnO (JCPDS NO. 36-1451) [21]. Here, the calculated ZnO nanoparticle size was ~5.6 nm based on its (1 1 0) peak according to Scherrer equation [22], which was in accordance with measured HRTEM result. The sharp diffraction pattern in S-3DOMPPy@ZnO represented the orthorhombic phase sulfur (PDF#08-024), indicating sulfur was successfully incorporated into the composite. The Fourier Transform infrared spectroscopy (FTIR) revealed that, in addition to C=C bond, there are four C-N bonds in 3DOMPPy and 3DOMPPy@ZnO (Fig. 4b). As mentioned before, the C-N sites played an important role in following advantages: *i)* a strong bonding for lithium polysulfide; *ii)* active sites for hosting ZnO nanocrystals. It not only helped relieve shuttle effect of polysulfides, but also favoured the growth and stabilization of ZnO ultra-fine nanocrystals. The content of 3DOMPPy and sulfur content were determined by TGA as seen in Fig. 4(c, d). The 3DOMPPy content up to 77.8 wt% in 3DOMPPy@ZnO composite can be analyzed from Fig. 4c. In the TGA curve of S-3DOMPPy@ZnO composite, there was a continuous weight decrease of

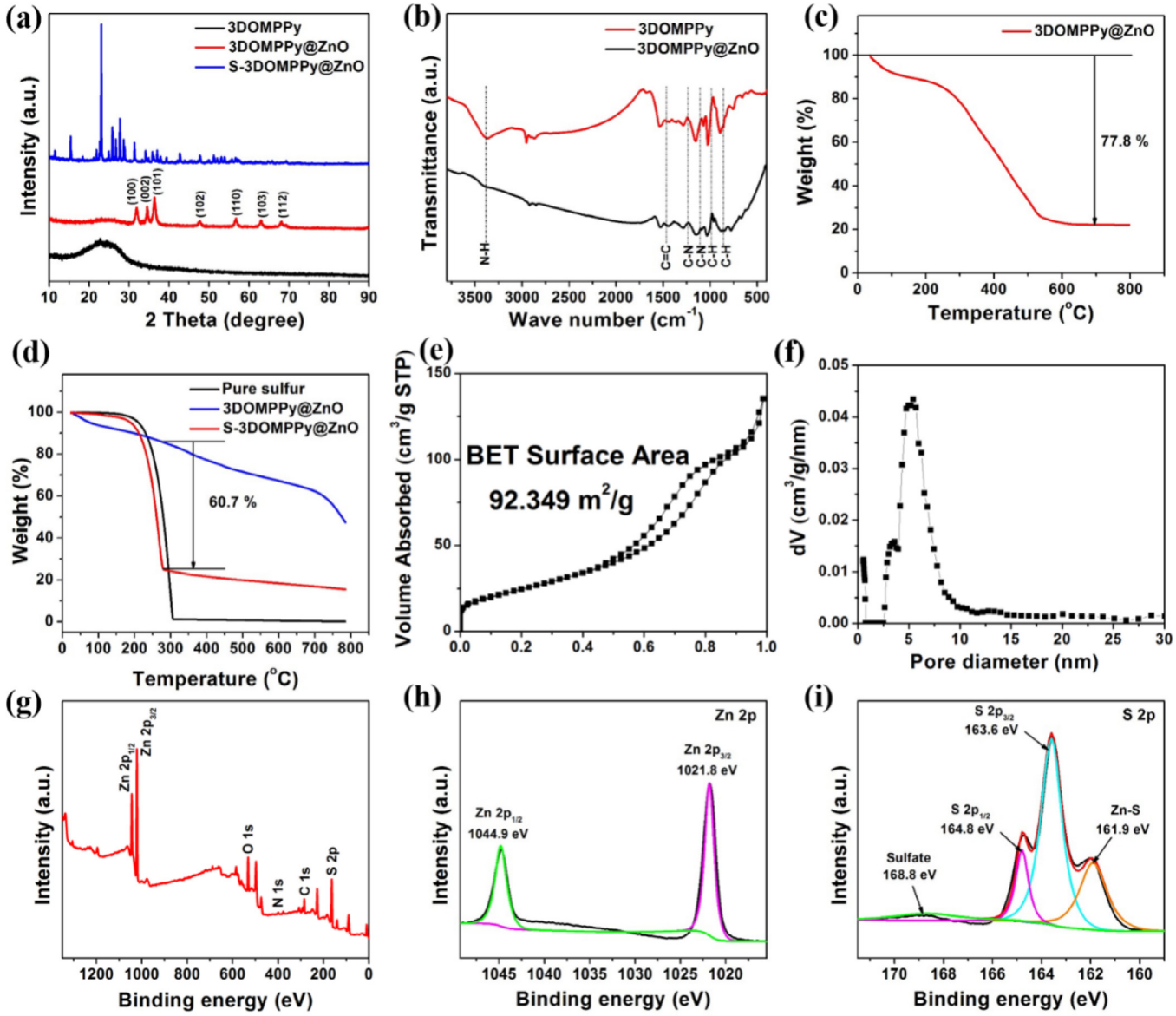

Fig. 4. (a) XRD patterns of 3DOMPPy, 3DOMPPy@ZnO and S-3DOMPPy@ZnO; (b) FTIR spectra of 3DOMPPy and 3DOMPPy@ZnO; TGA curve of (c) 3DOMPPy@ZnO composite in air; (d) Pure sulfur, 3DOMPPy@ZnO and S-3DOMPPy@ZnO composite under Ar atmosphere; (e) Nitrogen adsorption/desorption isotherms and (f) pore size distributionthe of the 3DOMPPy@ZnO composite; XPS spectra of (g) survey, (h) Zn 2p and (i) S 2p of the S-3DOMPPy@ZnO composite.

3DOMPPy@ZnO at 100 °C in Fig. 4d, subsequently, sulfur and 3DOMPPy shown a quality loss simultaneously. The first weight loss from 40 °C to 100 °C was explained as the evaporation of residual moisture. The mass loss at 100 °C was for the collapse of the 3DOMPPy. Evidently, sulfur thoroughly vanished at 300 °C, so the content of sulfur in S-3DOMPPy@ZnO was calculated to be 60.7%. It was worth noting that the evaporated temperature of sulfur in S-3DOMPPy@ZnO was lower than pure sulfur sample due to the uniform dispersion of nano-sized sulfur in S-3DOMPPy@ZnO compared to the bulk sulfur [23]. Nitrogen adsorption/desorption isotherms and pore size distribution of the 3DOMPPy@ZnO composite were shown in Fig. 4 (e, f). The high specific surface area (92.349 m^2/g) and uniform pore size distribution (~6.42 nm) have significant positive effect on the loading of sulfur, which leads to excellent electrochemical performance. The chemical states of S-3DOMPPy@ZnO had been characterized by XPS as shown in Fig. 4 (g-i). The Zn 2p spectrum can be fitted into Zn $2p_{3/2}$ (1021.8 eV) and Zn $2p_{1/2}$ (1044.9 eV) states, respectively. The S 2p spectrum in Fig. 4i can be deconvoluted into four peaks at 161.9, 163.6, 164.8, and 168.8 eV, corresponding to Zn-S, S-S $2p_{3/2}$, S-S $2p_{3/1}$, and sulfate bonds, respectively. The sulphate species was caused by the oxidation of sulfur. The strong Zn-S peak implied the polar interactions between Zn and S can effectively adsorb lithium polysulfide, which alleviated shuttle effect during the reaction.

The electrochemistry performance of S-3DOMPPy@ZnO was characterized by galvanostatic discharge-charge tests. Fig. 5a showed the discharge–charge voltage profiles at 1st, 50th, 100th, 200th, and 300th cycle between 1.5 and 3.0 V at 0.1 C. It was clear to see all the discharge–charge curves delivered two obvious discharge plateaus at 2.34 V and 2.06 V, which was ascribed to the formation of the dissoluble long-chain lithium polysulfide (Li_2S_n, $4 \le n \le 8$) and further insoluble Li_2S_2 or Li_2S, respectively. At the same time, even after 300 cycles, the position of the platform where the redox reaction was placed did not substantially change, indicating that the shuttle effect of the S-3DOMPPy@ZnO electrode was significantly suppressed. Furthermore, the initial discharge capacity was 1053.2 mAh g^{-1} and the coulombic efficiency of S-3DOMPPy@ZnO reached approximately 100% throughout the 300 cycles (Fig. 5b). The retention capacity after 300 cycling was 794.5 mAh g^{-1}, which represented a capacity reservation

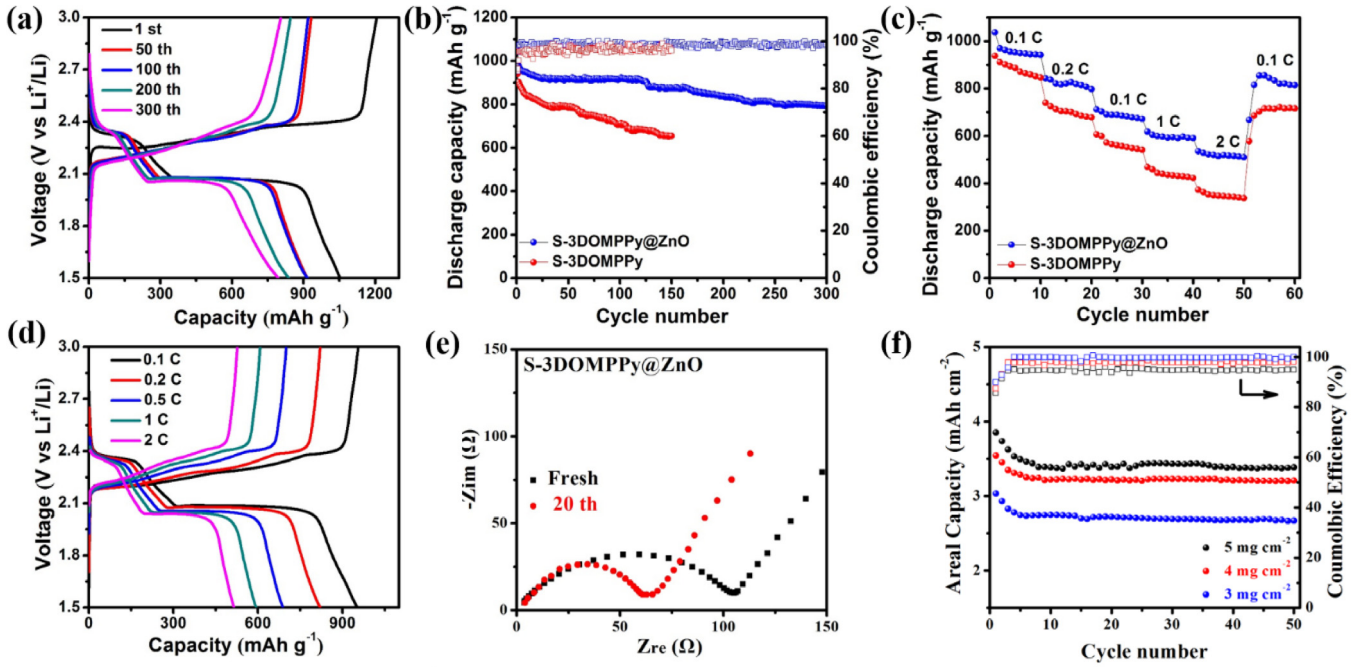

Fig. 5. (a) Discharge/charge voltage profiles of S-3DOMPPy@ZnO electrode for the 1 st, 50 th, 100 th, 200 th, and 300 th cycles at 0.1 C; (b) Cycle performance of S-3DOMPPy@ZnO and S-3DOMPPy electrodes; (c) Rate capability of S-3DOMPPy@ZnO and S-3DOMPPy electrodes; (d) Discharge/charge voltage profiles of S-3DOMPPy@ZnO electrode at different current density; (e) electrochemical impedance spectroscopy plots of S-3DOMPPy@ZnO cathodes; (f) Cycle performance of S-3DOMPPy@ZnO electrodes with different sulfur loading.

of 81%, demonstrating a suppression of the shuttle effect and an enhanced cycling stability. The capacity attenuation was primarily for the decomposition of electrolyte and production of the solid/electrolyte interphase.

Moreover, Fig. 5c presented the rate performances of the S-3DOMPPy@ZnO and S-3DOMPPy electrode at various current rates. The specific capacities of 952.3 (0.1 C), 821.5 (0.2 C), 689.1 (0.5 C), 593.2 (1 C) and 515.6 (2 C) mAh g^{-1} were delivered, when the c-rate brought back to 0.1 C after 50 cycles, 845.3 mAh g^{-1} was reached, showing the good rate performance of S-3DOMPPy@ZnO. Additionally, the discharge–charge voltage profiles from 0.1 C to 2 C also have been performed (Fig. 5d). After 300 cycles, the discharge plateaus still remain stable and overlapping at different current densities, indicating S-3DOMPPy@ZnO possessed highly reversible redox reactions and fast reaction kinetics. To confirm the improved electrochemical performance, electrochemical impedance spectroscopy (EIS) analysis of S-3DOMPPy@ZnO electrode was performed in Fig. 5e. After twenty cycles, the impedance value decreased significantly, indicating that the active substance was activated and resulted in a much faster interfacial charge transfer. Cycle performance of S-3DOMPPy@ZnO electrodes with different sulfur loading were observed at 3, 4, 5 mg cm^{-2}, respectively (Fig. 5f). 2.7, 3.2, 3.4 mAh cm^{-2} were achieved at 3, 4, 5 mg cm^{-2}, which demonstrated the advantages of 3DOMPPy@ZnO as sulfur host.

The excellent electrochemical properties of S-3DOMPPy@ZnO cathode was likely attributed to the synergetic effect between ZnO and 3DOMPPy: ZnO not only enhanced the trapping ability for lithium polysulfide, but also constructed polythionate complex serving as active site for redox reaction during the cycling; 3DOMPPy can provide continuous channels for electron transport, and act as reservoir to confine sulfur. Besides, it accommodated the volume expansion during long term cycling.

To explore the Lithium polysulfide adsorption abilities, 3DOMPPy and 3DOMPPy@ZnO were put into as-prepared Li_2S_6 solution (Fig. 6a). 3DOMPPy relied solely on weak physical adsorption, and the adsorption capacity for lithium polysulfide was not strong enough. In

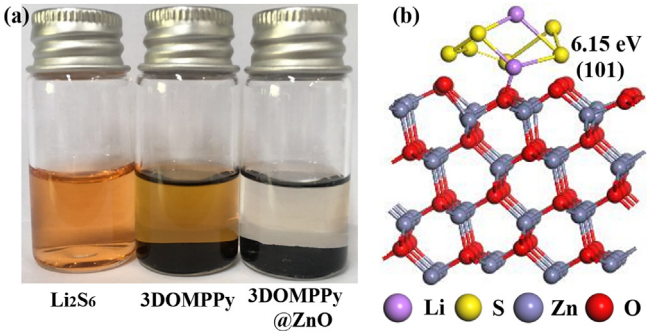

Fig. 6. (a) Lithium polysulfide adsorption of 3DOMPPy and 3DOMPPy@ZnO which were immersed in 4 mM Li_2S_6 solution, (b) Optimized configuration and the corresponding binding energy of Li_2S_6 on ZnO (1 0 1) surface.

3DOMPPy@ZnO, the physical adsorption capacity of 3DOMPPy was added to the chemisorption capacity of ZnO, and the two acted together to produce significant adsorption for lithium polysulfide. To further document the chemical adsorption of ZnO on Lithium polysulfide, the binding energy (E_b) of the lithium polysulfide on the (1 0 1) surface was explored using DFT calculations. The Li_2S_6 was used as the models for the lithium polysulfide species in this work. As shown in Fig. 6b, the E_b reaches a relative high adsorption energy value of 6.15 eV by forming the Li-O bonds between ZnO and Li_2S_6, which indicated that ZnO can more efficiently prevent the dissolution of lithium polysulfide.

Fig. 7 (a-b) showed the contact angle measurement before and after loading ZnO crystals, the results revealed 3DOMPPy@ZnO composite possessed a smaller contact angle (23.1°) compared with 3DOMPPy (34.6°), indicating the good electrolyte permeation of 3DOMPPy@ZnO composite and leading to rapid reaction of Li^+ with active material.

The performance of the S-3DOMPPy@ZnO cathode was compared with other reported results (Table 1). The results showed that the as prepared S-3DOMPPy@ZnO cathode exhibited a good cycle performance, delivering a high stable discharge specific capacity at 0.1 C and maintaining a low decay even at 300 cycles.

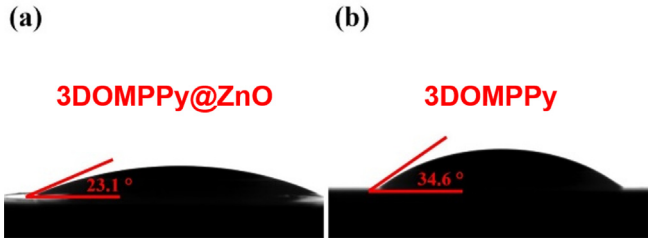

Fig. 7. Contact angle photographs of (a) 3DOMPPy@ZnO; (b) 3DOMPPy.

Table 1
Comparison of the electrochemical performance of previous reports with our work.

Electrode material	Sulfur loading (wt%)	Current density (discharge)	Reversible capacity (mAh g^{-1})	Cycle (No.)	Reference
AB/S/PPy	62	200 mA g^{-1}	577	100	[24]
S/Al_2O_3/PPy	67	200 mA g^{-1}	730	100	[25]
S@PPy	–	0.1 C	725	100	[26]
S-PPy	63.3	0.1 C	> 600	50	[27]
AB/S@PPy	67	0.2 C	769.3	80	[28]
S-3DOMPPy@ZnO	60.7	0.1 C	794.5	300	This work

4. Conclusion

In summary, building on our up-to-date understanding on the high activity of ultra-fine metal-based nanocrystals in catalysis, we developed a composite material consists of highly dispersed ultra-fine (~5 nm) ZnO nanocrystals decorated on conductive 3D porous PPy substrate. When the 3DOMPPy@ZnO was used as sulfur host, the porous 3DOMPPy ensured high conductivity, high sulfur utilization and fast sulfur kinetics. On the other hand, the small ZnO nanocrystals featured with polycrystalline surfaces ensured strong chemical bonding with Lithium polysulfide, which could effectively confine polysulfide. Profiting from the synergistic effect of 3D porous PPy and ultra-small ZnO, the S-3DOMPPy@ZnO cathode delivered a high reversible capacity of 794.5 mAh g^{-1} after 300 cycles at 0.1 C. The strategy presented in this study advanced the investigation of high-performance electrode material for Li/S batteries.

Acknowledgements

This work was supported by the financial support from the Program for the Outstanding Young Talents of Hebei Province, China; Cultivation project of National Engineering Technology Center [Grant No. 2017B090903008]; Ministry of Education and Science of the Republic of Kazakhstan via the Targeted Program BR05236524 “Innovative materials and systems for energy conversion and storage” and a Small Grant from Nazarbayev University “Development of safe and high performance flexible Li-ion batteries”.

References

[1] M. Li, J. Lu, Z. Chen, K. Amine, 30 years of lithium-ion batteries, Adv. Mater. 30 (2018) 1800561.
[2] Y. Zhang, P. Wang, Y. Yin, X. Zhang, L. Fan, N. Zhang, K. Sun, Heterostructured SnS-ZnS@C hollow nanoboxes embedded in graphene for high performance lithium and sodium ion batteries, Chem. Eng. J. 356 (2019) 1042–1051.
[3] T. Tao, S. Lu, Y. Fan, W. Lei, S. Huang, Y. Chen, Anode improvement in rechargeable lithium-sulfur batteries, Adv. Mater. 29 (2017) 1700542.
[4] Y. Zhang, Y. Zhao, Z. Bakenov, A simple approach to synthesize nanosized sulfur/graphene oxide materials for high-performance lithium/sulfur batteries, Ionics 20 (2014) 1047–1050.
[5] M. Kan, J. Yong, J. Feng, Y. Qian, S. Xiong, Hierarchical carbon nanotubes with a thick microporous wall and inner channel as efficient scaffolds for lithium-sulfur batteries, Adv. Funct. Mater. 26 (2016) 1571–1579.
[6] M. Xiang, W. Hao, H. Liu, H. Ju, H. Liu, A flexible 3D multifunctional MgO-decorated carbon foam@CNTs hybrid as self-supported cathode for high-performance lithium-sulfur batteries, Adv. Funct. Mater. 27 (2017) 1702573.
[7] X. Liu, J.Q. Huang, Q. Zhang, L. Mai, Nanostructured metal oxides and sulfides for lithium-sulfur batteries, Adv. Mater. 29 (2017) 1601759.
[8] M. Wang, L. Fan, D. Tian, X. Wu, Y. Qiu, C. Zhao, B. Guan, Y. Wang, N. Zhang, K. Sun, Rationally design hierarchical SnO_2/1T-MoS_2 nanoarray electrode for ultralong-life Li-S batteries, ACS Energy Lett. 3 (2018) 1627–1633.
[9] Y. Dong, S. Liu, Z. Wang, Y. Liu, Z. Zhao, J. Qiu, Sulfur-infiltrated graphene-backboned mesoporous carbon nanosheets with a conductive polymer coating for long-life lithium–sulfur batteries, Nanoscale 7 (2015) 7569–7573.
[10] B. Guan, L. Fan, X. Wu, P. Wang, Y. Qiu, M. Wang, Z. Guo, N. Zhang, K. Sun, The facile synthesis and enhanced lithium-sulfur battery performance of an amorphous cobalt boride (Co_2B)@graphene composite cathode, J. Mater. Chem. A 6 (2018) 24045–24049.
[11] A. Razzaq, Y. Yao, R. Shah, P. Qi, L. Miao, M. Chen, X. Zhao, Y. Peng, Z. Deng, High-performance lithium sulfur batteries enabled by a synergy between sulfur and carbon nanotubes, Energy Storage Mater. 16 (2019) 194–202.
[12] J. Jia, K. Wang, X. Zhang, X. Sun, H. Zhao, Y. Ma, Graphene-based hierarchically micro/mesoporous nanocomposites as sulfur immobilizers for high-performance lithium-sulfur batteries, Chem. Mater. 28 (2016) 7864–7871.
[13] F. Li, M.R. Kaiser, J. Ma, Z. Guo, H. Liu, J. Wang, Free-standing sulfur-polypyrrole cathode in conjunction with polypyrrole-coated separator for flexible Li-S batteries, Energy Storage Mater. 13 (2018) 312–322.
[14] X. Liang, M. Zhang, M.R. Kaiser, X. Gao, K. Konstantinov, R. Tandiono, Z. Wang, H.-K. Liu, S.-X. Dou, J. Wang, Split-half-tubular polypyrrole@sulfur@polypyrrole composite with a novel three-layer-3D structure as cathode for lithium/sulfur batteries, Nano Energy 11 (2015) 587–599.
[15] Y. Liu, W. Yan, X. An, X. Du, Z. Wang, H. Fan, S. Liu, X. Hao, G. Guan, A polypyrrole hollow nanosphere with ultra-thin wrinkled shell: synergistic trapping of sulfur in Lithium-Sulfur batteries with excellent elasticity and buffer capability, Electrochim. Acta 271 (2018) 67–76.
[16] F. Yin, X. Liu, Y. Zhang, Z. Yan, A. Menbayeva, Z. Bakenov, W. Xin, Well-dispersed sulfur anchored on interconnected polypyrrole nanofiber network as high performance cathode for lithium-sulfur batteries, Solid State Sci. 66 (2017) 44–49.
[17] E. Karaca, D. Gokcen, N. Pekmez, K. Pekmez, Electrochemical synthesis of PPy composites with nanostructured MnOx, CoOx, NiOx, and FeOx in acetonitrile for supercapacitor applications, Electrochim. Acta 305 (2019) 502–513.
[18] H. Li, Y. Wei, J. Ren, W. Zhang, C. Zhang, Y. Zhang, Three-dimensionally ordered hierarchically porous polypyrrole loading sulfur as high-performance cathode for lithium/sulfur batteries, Polymer 137 (2018) 261–268.
[19] C. Zhang, Z. Zheng, D. Wang, F. Yin, Y. Zhang, Three-dimensionally ordered macro-/mesoporous carbon loading sulfur as high-performance cathodes for lithium/sulfur batteries, J. Alloy. Compd. 714 (2017) 126–132.
[20] Y. Zhang, J. Ren, D. Wang, C. Zhang, F. Yin, A. Mukanova, Z. Bakenov, Sulfur-infiltrated three-dimensionally ordered mesoporous polypyrrole cathode for high-performance lithium-sulfur battery, ChemElectroChem 5 (2018) 1591–1598.
[21] Y. Zhang, Y. Wei, H. Li, Z. Yan, F. Yin, W. Xin, Simple fabrication of free-standing ZnO/graphene/carbon nanotube composite anode for lithium-ion batteries, Mater. Lett. 184 (2016) 235–238.
[22] C. Xiao, S. Zhang, S. Wang, Y. Xing, R. Lin, W. Xin, W. Wang, ZnO nanoparticles encapsulated in a 3D hierarchical carbon framework as anode for lithium ion battery, Electrochim. Acta 189 (2016) 245–251.
[23] X. Li, M. Rao, H. Lin, D. Chen, Y. Liu, S. Liu, Y. Liao, L. Xing, M. Xu, W. Li, Sulfur loaded in curved graphene and coated with conductive polyaniline: preparation and performance as a cathode for lithium-sulfur batteries, J. Mater. Chem. A 3 (2015) 18098–18104.
[24] S. Li, H. Li, G. Zhu, B. Jin, H. Liu, Q. Jiang, Improved electrochemical performance of Li-S battery with carbon and polymer-modified cathode, Appl. Surf. Sci. 479 (2019) 265–272.
[25] J. Xu, B. Jin, H. Li, Q. Jiang, Sulfur/alumina/polypyrrole ternary hybrid material as cathode for lithium-sulfur batteries, Int. J. Hydrogen Energy 42 (2017) 20749–20758.
[26] Y. Xie, H. Zhao, H. Cheng, C. Hua, W. Fang, J. Fang, J. Xu, Z. Chen, Facile large-scale synthesis of core–shell structured sulfur@polypyrrole composite and its application in lithium–sulfur batteries with high energy density, Appl. Energy 175 (2015) 522–528.
[27] Y. Fu, A. Manthiram, Orthorhombic bipyramidal sulfur coated with polypyrrole nanolayers as a cathode material for lithium − sulfur batteries, J. Phys. Chem. C 116 (2012) 8910–8915.
[28] W. Yang, W. Yang, J. Feng, X. Qin, A polypyrrole-coated acetylene black/sulfur composite cathode material for lithium–sulfur batteries, J. Energy Chem. 27 (2017) 813–819.